

Compressing the Channels in the Crystal Structure of Copper Squarate Metal-Organic Framework

Francisco Colmenero ^{1,2,*} , Álvaro Lobato ¹  and Vicente Timón ²

¹ Department of Chemical-Physics, Facultad de Ciencias Químicas, Universidad Complutense de Madrid, 28040 Madrid, Spain; a.lobato@ucm.es

² Instituto de Estructura de la Materia, Consejo Superior de Investigaciones Científicas, 28006 Madrid, Spain; vicente.timon@csic.es

* Correspondence: francolm@ucm.es

Abstract: The crystal structure of a copper squarate metal-organic framework is fully determined using first principles methods based in density functional theory. The compressibility of this material is studied by optimizing the structure under different isotropic pressures and uniaxial stresses directed along the direction of minimum compressibility, [1 0 0]. Under isotropic compression, channels become wider along [1 0 0], leading to negative linear compressibility, NLC. Under compression along [1 0 0], the unit-cell volume increases leading to negative volumetric compressibility.

Keywords: copper squarate; metal organic frameworks; crystal structure; elasticity; compressibility functions; negative linear compressibility



Citation: Colmenero, F.; Lobato, Á.; Timón, V. Compressing the Channels in the Crystal Structure of Copper Squarate Metal-Organic Framework. *Solids* **2022**, *3*, 374–384. <https://doi.org/10.3390/solids3020026>

Academic Editor: Timothy J. Prior

Received: 28 May 2022

Accepted: 16 June 2022

Published: 18 June 2022

Publisher's Note: MDPI stays neutral with regard to jurisdictional claims in published maps and institutional affiliations.



Copyright: © 2022 by the authors. Licensee MDPI, Basel, Switzerland. This article is an open access article distributed under the terms and conditions of the Creative Commons Attribution (CC BY) license (<https://creativecommons.org/licenses/by/4.0/>).

1. Introduction

The isotropic negative linear compressibility (INLC) phenomenon [1,2] is an important counterintuitive effect observed in materials that expand when compressed or shrink under tension. Under the effect of isotropic pressure (P), the total volume (V) of a thermodynamically and mechanically stable space-unconstrained [3] material should decrease. Therefore, the isotropic volumetric compressibility, $k_V = -1/V \cdot (\partial V / \partial P)_P$, should always be positive. This law, however, does not hold for each dimension of the material considered, and one or two of its dimensions (negative area compressibility) can increase under isotropic pressure if the remaining dimensions and the total volume decrease. In this case, the linear compressibility along a certain direction ℓ , $k_\ell = -1/\ell \cdot (\partial \ell / \partial P)_P$, can be negative. The anisotropic negative volumetric compressibility (ANVC) effect occurs when compression is not isotropic [4–8]. If a uniaxial stress is exerted along a certain direction m (P_m), the total volume can increase and the volumetric compressibility $k_V^m = -1/V \cdot (\partial V / \partial P_m)_P$ can be negative. Materials exhibiting negative compressibilities, frequently simultaneously displaying the negative Poisson's ratio (NPR) phenomenon [9–11], have been proposed for an immense range of potential applications, such as the development of ultrasensitive pressure-sensing devices [1,12], pressure driven actuators [12,13], optical telecommunication cables [1], artificial muscles [14] and body armor [12,15], and for sound attenuation [16], superconductivity modulation [17], ferroelectric enhancement [1] and transmission stabilization [18]. The main difficulties encountered in the practical applications of the natural and man-made NLC materials that have been found to date, is the relatively small absolute value of their negative compressibilities and the short range of pressure for which NLC effects are displayed. Thus, even though the search for new NLC materials has been intense and fruitful [2], the investigation is still in a highly active state. One of the main lines of research concerns the underlying structural mechanisms of the NLC phenomenon because, in most cases, the presence of NLC effects is a direct consequence of the structural characteristics. The use of these structure-function relationships should simplify the search for NLC materials, for example by filtering the crystal structures displaying these structural motifs.

Furthermore, since nanotechnology promises the construction of materials with almost any requested geometry, the artificial reproduction of the structural motifs leading to NLC with variable compositions should allow one to generate a wide range of metamaterials [19] with desirable mechanical properties. Some of the known NLC mechanisms are the presence of ferroelastic instabilities, phonon instabilities, ferroelastic phase transitions and the anomalous mechanical behavior found in materials displaying correlated polyhedral tilts and helical and wine-rack structural motifs [2]. NLC effects were also found in chain or sheet structures linked by means of van der Waals interactions [4,5] or in structures displaying rotating polygon structural motifs [20–22]. An additional NLC mechanism was recently found for the crystal structure of porous materials containing cylindrical channels [23,24]. The main objective of this work is to confirm that these types of highly flexible crystal structures are likely to exhibit NLC effects. Therefore, the structures of crystalline species containing a small number of chemical elements were filtered to find simple compounds displaying empty structural channels. Among the simplest structures found, one was that of copper squarate [25], Cu_4O_4 , a simple metal-organic framework, which fitted perfectly with the search pattern. Then, a study of the behavior of this compound under pressure was performed. A significant NLC effect was found, and the computed crystal structures under the effect of pressure very clearly showed an NLC mechanism based on the structural modification of the channels, which is the only source of the NLC effect in copper squarate.

2. Methods

Copper squarate was studied using first-principles solid-state methods based in Density Functional Theory using plane wave basis sets and pseudopotentials [26]. The CASTEP program [27] was employed for all the computations. The specialized version of the Perdew–Burke–Ernzerhof (PBE) energy-density functional for solid materials, PBEsol [28], was used. The good behavior of this functional for describing anhydrous materials has been widely recognized [29–36]. The pseudopotentials utilized for C, O and Cu atoms were standard norm-conserving pseudopotentials [37] provided in CASTEP code (00PBE-OP type). The optimization of the atomic positions and unit cell lattice parameters was carried out using the Broyden–Fletcher–Goldfarb–Shanno technique [38]. All the optimizations, even those of the compound under pressure, were performed with stringent convergence thresholds in the variation of the total energy, maximum atomic force, maximum atomic displacement and maximum stress of 2.5×10^{-6} eV/atom, 0.005 eV/Å, 2.5×10^{-4} and 0.0025 GPa, respectively, with the purpose of obtaining smooth pressure-volume curves. In the calculations, a large plane-wave kinetic energy cutoff ($\epsilon = 1000$ eV) and a dense k point mesh [39] ($3 \times 3 \times 5$, corresponding to a grid density of 0.04 \AA^{-1}), were employed. The elasticity matrix of copper squarate was determined for the optimized crystal structure using the method of finite deformations [40]. The methodology used in this paper has been employed successfully in many previous works [4–8,23,24,31,35,41,42] in order to describe the elastic response of solid materials. For example, the predicted anomalous mechanical behavior of silver oxalate [6] was recently verified experimentally [20].

3. Results

Copper squarate is monoclinic, space group $I2/a$ (No. 15) [25]. In this paper, the axes were reordered, and the standard setting $C2/c$ (No. 15) was adopted. The crystal structure of copper squarate was described in detail by Dinnebier et al. [25]. A view of the crystal structure from the $[0\ 0\ 1]$ crystallographic direction, clearly showing the presence of empty channels in the structure, is given in Figure 1. A single channel is explicitly shown by means of the corresponding solvent-accessible surface in a $1 \times 1 \times 5$ supercell in Figure 2. The calculated unit-cell parameters of copper squarate are given in Table 1, and the calculated interatomic distances and angles are given in Tables S1 and S2 of the Supplementary Material (SM), respectively. In these tables, the calculated values are compared with the corresponding experimental data [25]. It must be noted that a full structure determination of the crystal structure of copper squarate was not possible in the

work by Dinnebier et al. [25]. These authors performed a rigid-body Rietveld refinement of the squarate anions without a determination of the corresponding internal degrees of freedom. Therefore, the fully optimized structure obtained in this work is reported in the SM as a file with a CIF (Crystallographic Information File) format. As can be observed in Table 1, the difference in the computed unit cell volume using the PBE functional with respect to the experimental value of Dinnebier et al. [25] is very large, 10.0%. The results were significantly improved when the PBEsol functional was used. The difference was reduced to 4.6%. The PBE functional supplemented with dispersion corrections [43] and several hybrid energy-density functionals, such as the PBE0 [44] and B3LYP [45] ones, was also used but led to larger differences in the computed unit cell volume and parameters with respect to the experiment. Therefore, the PBEsol functional was selected to determine the mechanical properties of copper squarate. The X-ray powder diffraction pattern of copper squarate was determined from the computed and experimental structures [46]. The results are compared in Figure S2 of the SM, and, as can be seen, they are in good agreement. The positions of the main reflections in the computed and experimental X-ray powder patterns are compared in Table S3 of the SM.

The rigid-body Rietveld refinement of the squarate anions [25] provided average bond lengths for the C-C (1.23 Å) and C-O (1.45 Å) bonds, which agreed reasonably with experimental values of these bond lengths reported in the literature. For comparison, the different C-C bond lengths in squaric acid lead to an average C-C distance of 1.46 Å, and the corresponding C-O bond lengths give an average C-O distance of 1.26 Å [4,47]. The computed C1-C2 and C1-C2' bond distances (see Table S1) differ from the average value by about 0.04 Å. Similarly, the differences for the calculated C1-O1 and C2-O2 distances are smaller than 0.02 Å. Finally, the Cu-O1, Cu-O2 and Cu-O2' distances agree with their experimental counterparts within about 0.1 Å. Due to the incomplete structure refinement, the computed C-C-C and O-C-C angles should not be compared with the corresponding experimental values. However, the theoretical O-Cu-O angles are in reasonable agreement with the experiment [25].

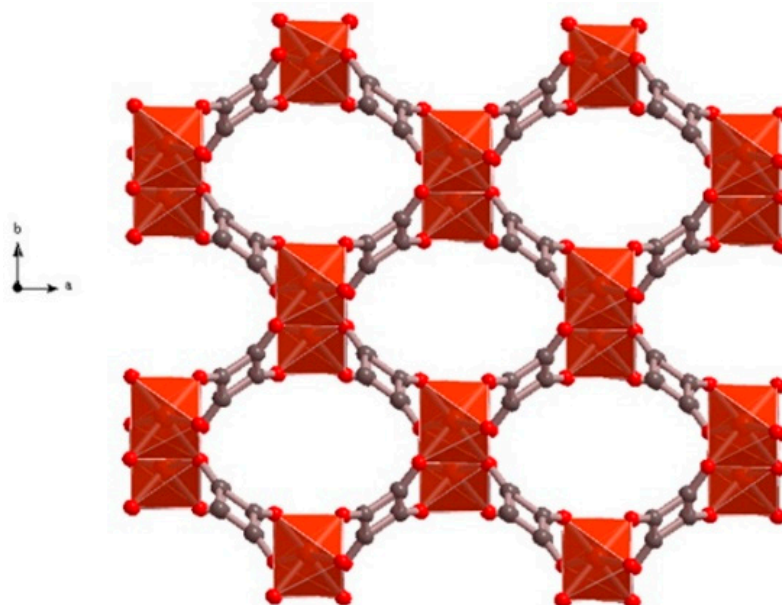


Figure 1. Computed crystal structure of copper squarate: view of a $2 \times 2 \times 2$ supercell from [0 0 1] direction. Color code: Cu—orange; C—gray; O—red.

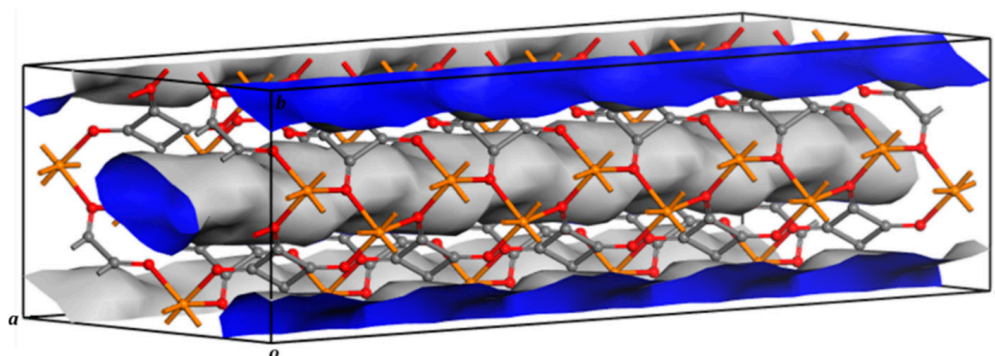


Figure 2. A channel in the crystal structure of copper squarate displayed by means of the corresponding solvent-accessible surface in a $1 \times 1 \times 5$ supercell.

Table 1. Lattice parameters of copper squarate.

| Parameter | $a(\text{\AA})$ | $b(\text{\AA})$ | $c(\text{\AA})$ | α (deg) | β (deg) | γ (deg) | Vol. (\AA^3) | $\rho(\text{gr}/\text{cm}^3)$ |
|------------|-----------------|-----------------|-----------------|----------------|---------------|----------------|-------------------------|-------------------------------|
| PBE | 11.1926 | 9.1271 | 5.7595 | 90.0 | 116.07 | 90.0 | 528.5049 | 2.207 |
| PBE + disp | 11.1578 | 9.1640 | 5.5982 | 90.0 | 117.78 | 90.0 | 506.4448 | 2.303 |
| B3LYP | 11.1829 | 9.2835 | 5.9160 | 90.0 | 114.88 | 90.0 | 557.1953 | 2.093 |
| PBEsol | 11.0961 | 9.0074 | 5.6076 | 90.0 | 116.26 | 90.0 | 502.6355 | 2.320 |
| Exp. [25] | 10.6869(4) | 8.9394(4) | 5.6747(1) | 90.0 | 117.60(2) | 90.0 | 480.4546 | 2.427 |

The computed elasticity matrix of copper squarate is:

$$C = \begin{pmatrix} 72.78 & 44.11 & 38.74 & 0.00 & -25.81 & 0.00 \\ 44.11 & 44.30 & 19.38 & 0.00 & -2.61 & 0.00 \\ 38.74 & 19.38 & 52.31 & 0.00 & -17.54 & 0.00 \\ 0.00 & 0.00 & 0.00 & 14.24 & 0.00 & -4.70 \\ -25.81 & -2.61 & -17.54 & 0.00 & 30.60 & 0.00 \\ 0.00 & 0.00 & 0.00 & -4.70 & 0.00 & 32.78 \end{pmatrix} \quad (1)$$

In this equation all values are given in GPa. The mechanical stability of its structure was analyzed from the computed elasticity matrix. According to the necessary and sufficient Born stability condition [48], if a material is mechanically stable, the elasticity matrix should be positive definite, i.e., all its eigenvalues must be positive. Therefore, the elasticity matrix of copper squarate was diagonalized numerically. Since all the eigenvalues were found to be positive, copper squarate is mechanically stable. The mechanical properties of copper squarate were then evaluated as a function of the orientation of the applied stress, and tridimensional representations were performed using ELAM software [49]. The results are shown in Figure S3 of the SM. Bidimensional projections on the xy and xz planes are given in Figures 3 and 4, respectively. As can be observed in Figure 4A, copper squarate exhibits negative compressibilities for a wide range of directions of the applied stress. The direction of minimum compressibility is close to $[1 \ 0 \ 0]$. Furthermore, Figure 4D shows that copper squarate displays the negative Poisson's ratio phenomenon. The minimum value of the Poisson's ratio is quite significant, $\nu_{min} = -0.66$, for an external stress applied along the minimum Poisson's ratio direction, $[-0.43, -0.36, +0.82]$.

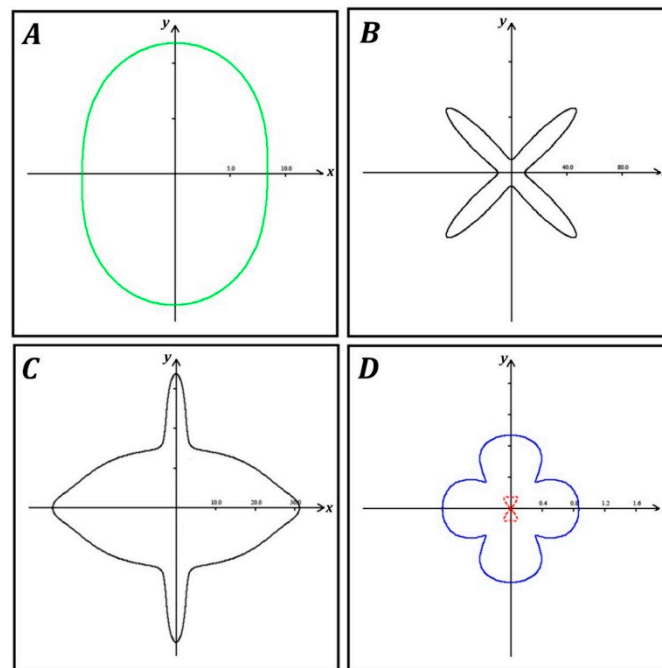


Figure 3. Two-dimensional projections on the xy plane of the tridimensional representations of the elastic properties of copper squarate as a function of the orientation of the applied stress: (A) Compressibility; (B) Young modulus; (C) Maximum shear modulus; (D) Maximum (blue) and minimum (red) Poisson's ratios. The labels of the marks in the vertical axis are exactly the same as those of the horizontal one. In the plots, negative values are displayed in red.

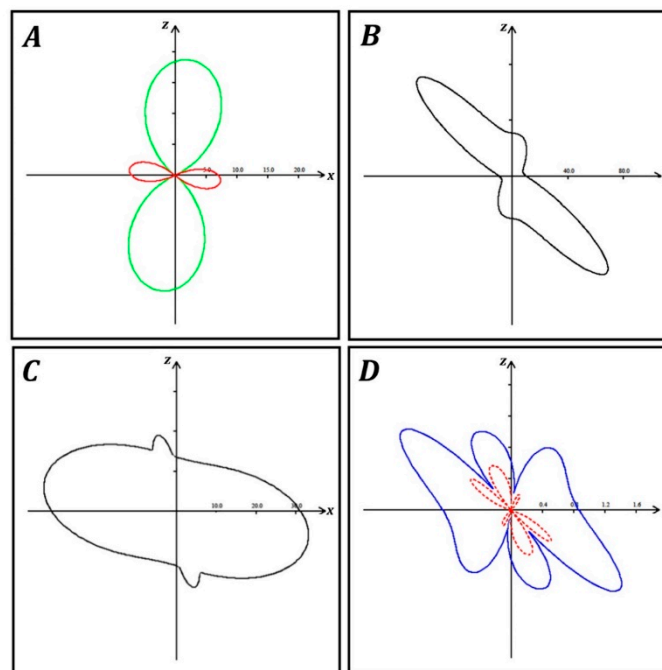


Figure 4. Two-dimensional projections on the xz plane of the tridimensional representations of the elastic properties of copper squarate as a function of the orientation of the applied stress: (A) Compressibility; (B) Young modulus; (C) Maximum shear modulus; (D) Maximum (blue) and minimum (red) Poisson's ratios. The labels of the marks in the vertical axis are exactly the same as those of the horizontal one. In the plots, negative values are displayed in red.

The crystal structure of copper squarate was optimized under the effect of twenty-one different isotropic pressures in the range of -1.50 to 6.00 GPa. The optimized unit cell volumes and lattice parameters are plotted in Figure 5 and given in Table S4 of the SM. As can be seen in Figure 5B, the a lattice parameter increases significantly from the lowest isotropic pressure considered, $p = -1.50$ GPa, up to $p = 4.14$ GPa. Therefore, copper squarate exhibits the INLC phenomenon in this pressure range. The b and c lattice parameters and the total unit-cell volume decrease. The computed compressibilities are shown in Figure 5E and given in Table S5 of the SM. The minimum value of the compressibility is found for $P = 1.35$ GPa, $k_a = -8.14$ TPa $^{-1}$. Although a large variation of the unit cell volume and parameters is observed between 1.0 and 2.0 GPa, no topological changes on the bond structure were observed, and, therefore, copper squarate does not undergo a pressure-induced phase transition in this region. Furthermore, the enthalpy pressure equation of state (Figure S4 of the SM) does not show any slope change, ruling out phase transitions within the complete range of pressure considered.

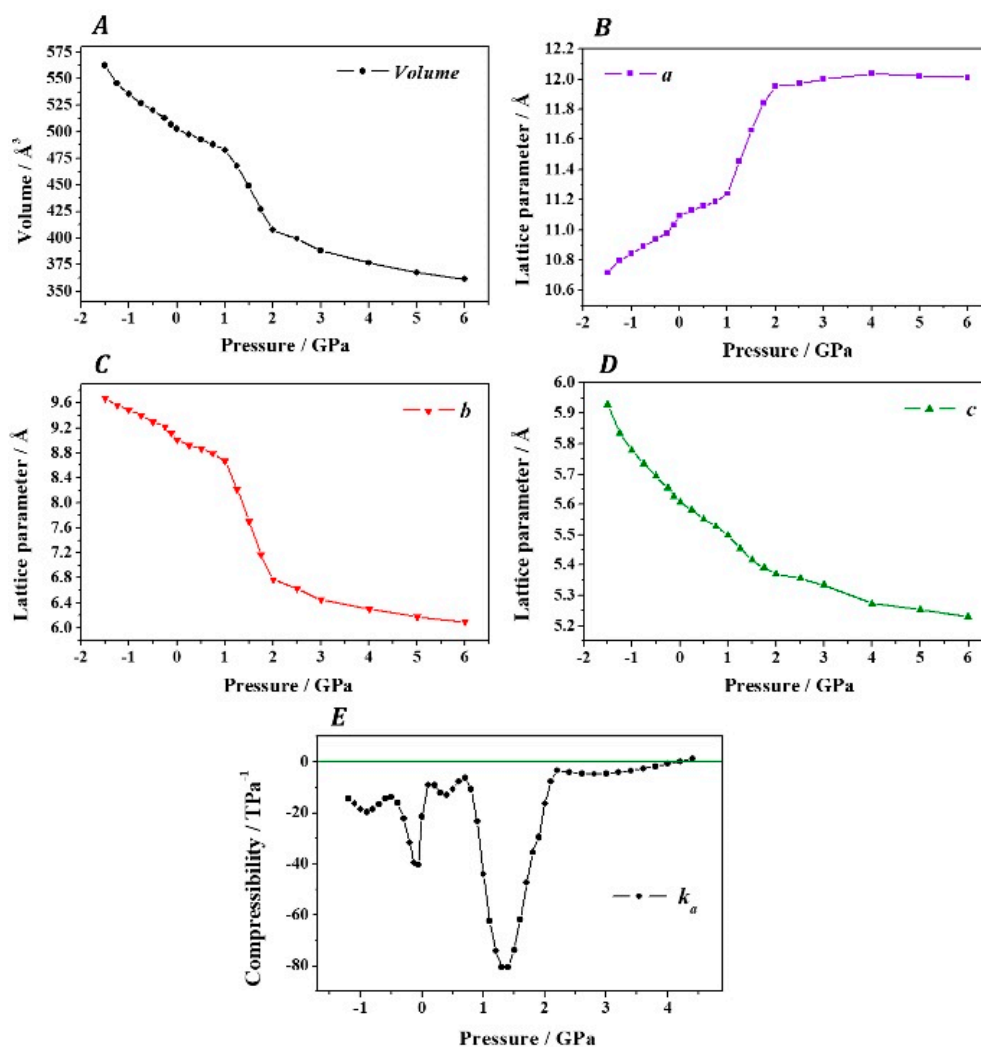


Figure 5. (A) Computed unit cell volume of copper squarate as a function of the applied isotropic pressure; (B) a lattice parameter; (C) b lattice parameter; (D) c lattice parameter; (E) Compressibility along $[1\ 0\ 0]$ crystallographic direction, $k_a = -1/a \cdot (\partial a / \partial P)_P$.

The structure of CuC_4O_4 was also optimized under the effect of eleven different stresses applied in the minimum compressibility direction, $[1\ 0\ 0]$, in the range going from $P = -0.33$ to $P = 0.25$ GPa. The corresponding optimized unit cell volumes and lattice parameters are plotted in Figure 6 and given in Table S6 of the SM. Figure 6A shows that

the unit-cell volume increases from $P = -0.33$ GPa to $P = 0.17$ GPa. Hence, copper squarate displays the ANVC phenomenon in this pressure range. The calculated compressibilities are plotted in Figure 6E and given in Table S7 of the SM. The minimum value of the compressibility, $k_V = -1/V \cdot (\partial V / \partial P)_P = -81.3 \text{ TPa}^{-1}$, is obtained for $P = 0.12$ GPa.

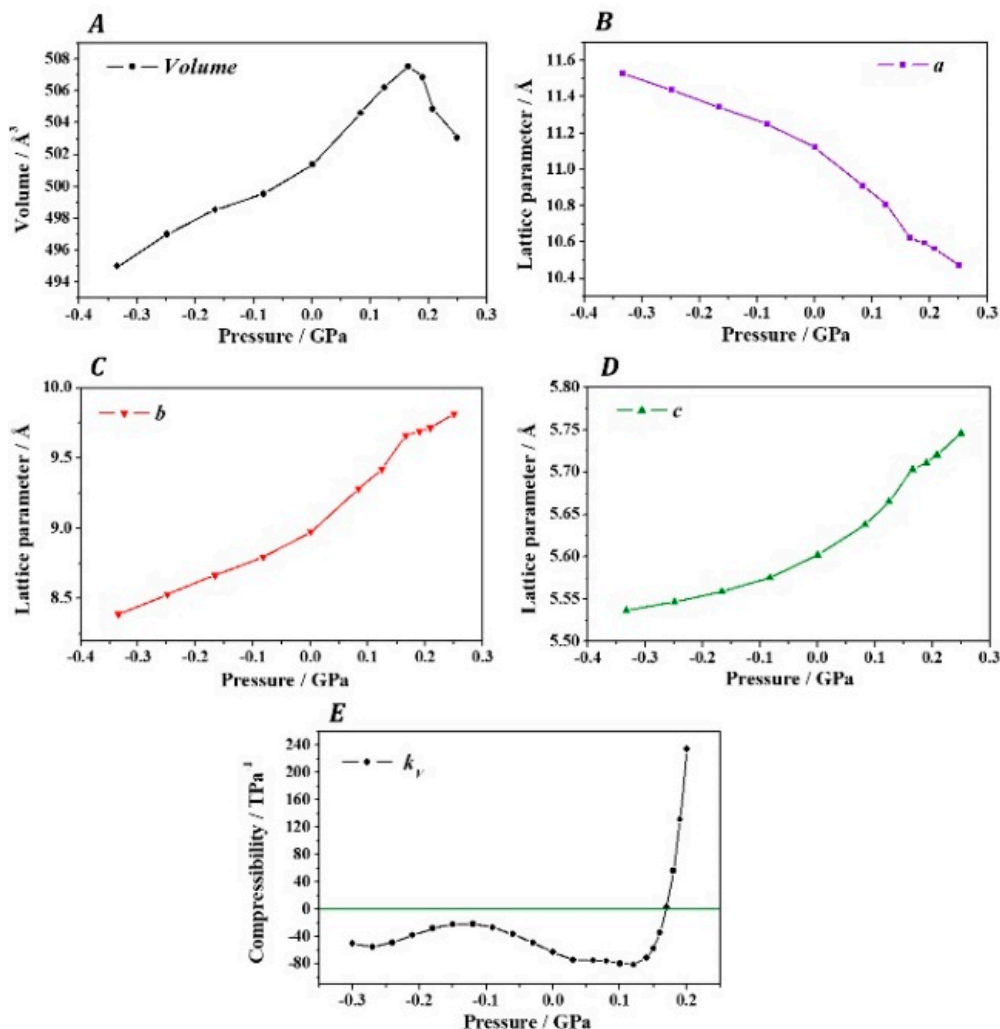


Figure 6. (A) Computed unit cell volume of copper squarate as a function of the external stress applied along the [1 0 0] crystallographic direction; (B) *a* lattice parameter; (C) *b* lattice parameter; (D) *c* lattice parameter; (E) Volumetric compressibility, $k_V = -1/V \cdot (\partial V / \partial P)_P$.

4. Discussion

The structural mechanism of INLC was studied by analyzing the variation of the optimized structures under isotropic pressure. As shown in Figure 7, the width and height of the channels become increasingly larger and smaller, respectively, under pressure. As a result, the *a* lattice parameter increases strongly, and the compressibility is negative for a wide pressure range. The more important structural change that is observed is the variation of the relative angle between the copper octahedra and the squarate rings. The variation of the Cu–O–C angle, mainly responsible for the largest peak in the compressibility found in Figure 5E, is reduced from 127.7° to 123.3° between $P = 1.0$ GPa and 2.0 GPa.

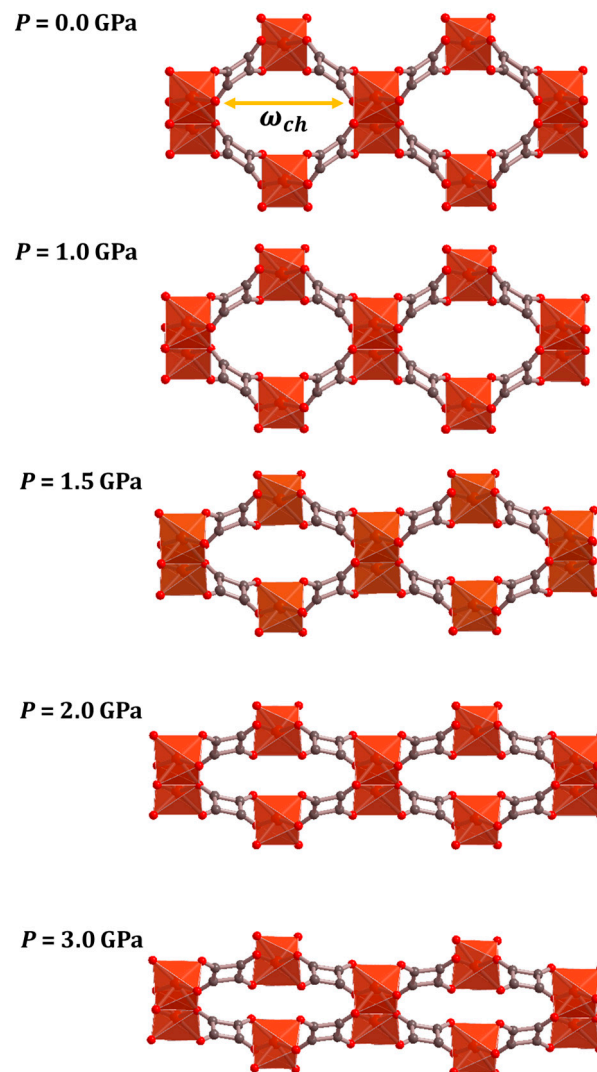


Figure 7. The structure of copper squarate under increasing isotropic pressures. View of a $2 \times 1 \times 1$ supercell from $[001]$ direction showing two structural channels at different pressures: $P = 0.0, 1.0, 1.5, 2.0$ and 3.0 GPa. The meaning of the width of a channel (ω_{ch}) as measured by the distance between two opposite oxygen atoms is illustrated in the structure at $P = 0.0$ GPa. The values of ω_{ch} are 8.154, 8.300, 8.810, 9.193 and 9.277, respectively.

Similarly, the mechanism of ANVC was revealed by analyzing the modification of the optimized structures under external stresses applied along the $[100]$ direction. As shown in Figure 8, contrary to the behavior of the crystal structure under isotropic pressure, the width and height of the channels become smaller and larger, respectively, as the stress increases and the total unit-cell volume increases. Therefore, the volumetric compressibility is negative.

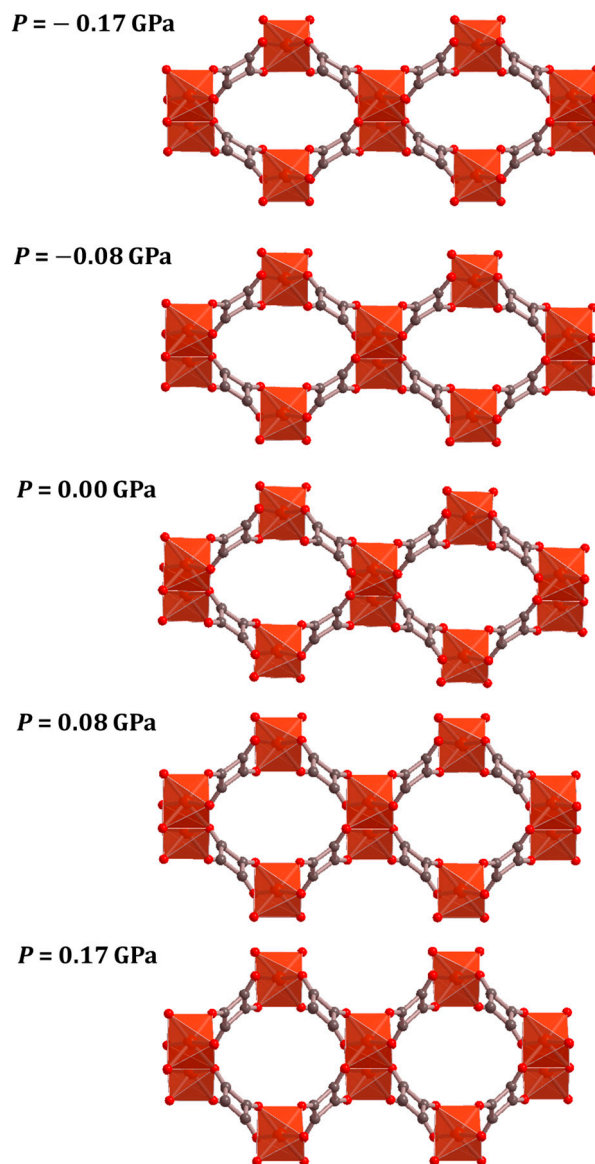


Figure 8. The structure of copper squarate under different stresses applied along $[1\ 0\ 0]$ direction. View of a $2 \times 1 \times 1$ supercell showing two structural channels at different stresses: $P = -0.17, -0.08, 0.0, 0.08$ and 0.17 GPa.

5. Conclusions

The isotropic compression of structures containing empty channels shows a clear trend for producing large NLC effects due to the elongation of the elliptic section of the channels along its major semi-axis accompanied by the reduction of its minor semi-axis. Under compression along the direction of the major semi-axis, however, the corresponding dimension of the unit cell is reduced and the minor semi-axis and total volume increase, leading to a negative volumetric compressibility. Similar results were obtained in previous studies [23,24]. Therefore, additional studies on the mechanical properties of an extended set of porous solid compounds containing the empty channel structural motif, such as other MOFS, zeolites and aluminophosphate materials, are now being carried out. The results obtained so far have shown that, essentially, the same behavior is obtained for a large fraction of the materials considered. The minimum isotropic compressibility of copper squarate was found to be significant, $k_a = -81.4\ \text{TPa}^{-1}$ at $P = 1.35$ GPa. The computed minimum anisotropic volumetric compressibility is $k_V = -81.3\ \text{TPa}^{-1}$ at $P = 0.12$ GPa. The compressibility functions of copper squarate must be evaluated experimentally to confirm

the present theoretical results. Although the results of accurate non-empirical calculations are generally in agreement with the experiment [20], the study of the effect of temperature, pressure-transmitting media and a partial occupation of the channels with water could be very interesting.

Supplementary Materials: The following supporting information can be downloaded at: <https://www.mdpi.com/article/10.3390/solids3020026/s1>. The supplementary information associated with this article contains: (a) Interatomic distances and angles; (b) X-ray diffraction pattern; (c) Tridimensional representations of the mechanical properties; (d) Unit-cell volumes, lattice parameters and compressibilities under isotropic pressures and uniaxial stresses. Ref. [25] is cited in the supplementary materials.

Author Contributions: Conceptualization: F.C.; Investigation: F.C., Á.L. and V.T.; Writing—original draft: F.C.; Writing—review & editing: F.C., Á.L. and V.T. All authors have read and agreed to the published version of the manuscript.

Funding: This work was financially supported by the Ministerio de Ciencia e Innovación (project PGC2018-094814-B-C21). V.T. was supported by the Ministry of Science, Innovation and Universities within the Project FIS2016-77726-C3-1-P.

Acknowledgments: Supercomputer time by the CTI-CSIC center is gratefully acknowledged. We want to thank A. M. Fernández for reading the manuscript and for many helpful comments.

Conflicts of Interest: The authors declare that they have no known competing financial interest or personal relationship that could have appeared to influence the work reported in this paper.

References

1. Baughman, R.H.; Stafström, S.; Cui, C.; Dantas, S.O. Materials with Negative Compressibilities in One or More Dimensions. *Science* **1998**, *279*, 1522–1524. [[CrossRef](#)] [[PubMed](#)]
2. Cairns, A.B.; Goodwin, L. Negative Linear Compressibility. *Phys. Chem. Chem. Phys.* **2015**, *17*, 20449–20465. [[CrossRef](#)] [[PubMed](#)]
3. Lakes, R.S.; Wojciechowski, K.W. Negative Compressibility, Negative Poisson's Ratio and Stability. *Phys. Stat. Sol.* **2008**, *245*, 545–551. [[CrossRef](#)]
4. Colmenero, F. Anomalous mechanical behavior of the deltic, squaric and croconic cyclic oxocarbon acids. *Mater. Res. Express* **2019**, *6*, 045610. [[CrossRef](#)]
5. Colmenero, F. Mechanical Properties of Anhydrous Oxalic Acid and Oxalic Acid Dihydrate. *Phys. Chem. Chem. Phys.* **2019**, *21*, 2673–2690. [[CrossRef](#)]
6. Colmenero, F. Silver Oxalate: Mechanical Properties and Extreme Negative Mechanical Phenomena. *Adv. Theor. Simul.* **2019**, *2*, 1900040. [[CrossRef](#)]
7. Colmenero, F.; Timón, V. Extreme negative mechanical phenomena in the zinc and cadmium anhydrous metal oxalates and lead oxalate dihydrate. *J. Mater. Sci.* **2020**, *55*, 218–236. [[CrossRef](#)]
8. Colmenero, F. Organic acids under pressure: Elastic properties, negative mechanical phenomena and pressure induced phase transitions in the lactic, maleic, succinic and citric acids. *Mater. Adv.* **2020**, *1*, 1399–1426. [[CrossRef](#)]
9. Lakes, R.S. Foam structures with a negative Poisson's ratio. *Science* **1987**, *235*, 1038–1040. [[CrossRef](#)]
10. Wojciechowski, K.W. Constant thermodynamic tension Monte Carlo studies of elastic properties of a two-dimensional system of hard cyclic hexamers. *Mol. Phys.* **1987**, *61*, 1247–1258. [[CrossRef](#)]
11. Lakes, R.S. Negative-Poisson's-ratio materials: Auxetic solids. *Annu. Rev. Mater. Res.* **2017**, *47*, 63–81. [[CrossRef](#)]
12. Nicolaou, Z.G.; Motter, A.E. Mechanical metamaterials with negative compressibility transitions. *Nat. Mater.* **2012**, *11*, 608–613. [[CrossRef](#)] [[PubMed](#)]
13. Spinks, G.M.; Wallace, G.G.; Fifield, L.S.; Dalton, L.R.; Mazzoldi, A.; De Rossi, D.; Khayrullin, I.; Baughman, R.H. Pneumatic Carbon Nanotube Actuators. *Adv. Mater.* **2002**, *14*, 1728–1732. [[CrossRef](#)]
14. Aliev, A.E.; Oh, J.; Kozlov, M.E.; Kuznetsov, A.A.; Fang, S.; Fonseca, A.F.; Ovalle, R.; Lima, M.D.; Haque, M.H.; Gartstein, Y.N.; et al. Giantstroke, superelastic carbon nanotube aerogel muscles. *Science* **2009**, *323*, 1575–1578. [[CrossRef](#)] [[PubMed](#)]
15. Evans, K.E.; Alderson, A. Auxetic Materials: Functional Materials and Structures from Lateral Thinking! *Adv. Mater.* **2000**, *12*, 617–628. [[CrossRef](#)]
16. Fang, N.; Xi, D.; Xu, J.; Ambati, M.; Srituravanich, W.; Sun, C.; Zhang, X. Ultrasonic metamaterials with negative modulus. *Nat. Mater.* **2006**, *5*, 452–456. [[CrossRef](#)]
17. Uhoya, W.; Tsoi, G.; Vohra, Y.K.; McGuire, M.A.; Sefat, A.S.; Sales, B.C.; Mandrus, D.; Weir, S.T. Anomalous compressibility effects and superconductivity of EuFe_2As_2 under high pressures. *J. Phys. Condens. Matter.* **2010**, *22*, 292202. [[CrossRef](#)]
18. Jiang, X.; Molokeev, M.S.; Dong, L.; Dong, Z.; Wang, N.; Kang, L.; Li, X.; Li, Y.; Tian, C.; Peng, S.; et al. Anomalous mechanical materials squeezing three-dimensional volume compressibility into one dimension. *Nat. Commun.* **2020**, *11*, 5593. [[CrossRef](#)]

19. Yu, X.; Zhou, J.; Liang, H.; Jiang, Z.; Wu, L. Mechanical metamaterials associated with stiffness, rigidity and compressibility: A brief review. *Prog. Mater. Sci.* **2018**, *94*, 114–173. [[CrossRef](#)]
20. Colmenero, F.; Jiang, X.; Li, X.; Li, Y.; Lin, Z. Negative area compressibility in silver oxalate. *J. Mater. Sci.* **2021**, *56*, 269–277. [[CrossRef](#)]
21. Grima-Cornish, J.N.; Vella-Zarb, L.; Grima, J.N. Negative Linear Compressibility and Auxeticity in Boron Arsenate. *Ann. Phys.* **2020**, *2020*, 1900550. [[CrossRef](#)]
22. Grima, J.N.; Evans, K.E. Auxetic behavior from rotating squares. *J. Mater. Sci. Lett.* **2020**, *19*, 1563–1565. [[CrossRef](#)]
23. Colmenero, F.; Sejkora, J.; Plášil, J. Crystal structure, infrared spectrum and elastic anomalies in tuperussuatsiaite. *Sci Rep.* **2020**, *10*, 7510. [[CrossRef](#)] [[PubMed](#)]
24. Colmenero, F. Negative linear compressibility in nanoporous metal–organic frameworks rationalized by the empty channel structural mechanism. *Phys. Chem. Chem. Phys.* **2021**, *23*, 8508–8524. [[CrossRef](#)] [[PubMed](#)]
25. Dinnebier, R.E.; Nuss, H.; Jansen, M. Anhydrous CuC_4O_4 , a Channel Structure solved from X-ray Powder Diffraction Data. *Z. Anorg. Allg. Chem.* **2005**, *63*, 2328–2332.
26. Payne, M.C.; Teter, M.P.; Ailan, D.C.; Arias, A.; Joannopoulos, J.D. Iterative minimization techniques for ab initio total-energy calculations: Molecular dynamics and conjugate gradients. *Rev. Mod. Phys.* **1992**, *64*, 1045–1097. [[CrossRef](#)]
27. Clark, S.J.; Segall, M.D.; Pickard, C.J.; Hasnip, P.J.; Probert, M.I.J.; Refson, K.; Payne, M.C. First Principles Methods Using CASTEP. *Z. Kristallogr.* **2005**, *220*, 567–570. [[CrossRef](#)]
28. Perdew, J.P.; Ruzsinszky, A.; Csonka, G.I.; Vydrov, O.A.; Scuseria, G.E.; Constantin, L.A.; Zhou, X.; Burke, K. Restoring the Density-Gradient Expansion for Exchange in Solids and Surfaces. *Phys. Rev. Lett.* **2008**, *100*, 136406. [[CrossRef](#)]
29. Bonales, L.J.; Colmenero, F.; Cobos, J.; Timón, V. Spectroscopic Raman Characterization of Rutherfordine: A Combined DFT and Experimental Study. *Phys. Chem. Chem. Phys.* **2016**, *18*, 16575–16584. [[CrossRef](#)]
30. Colmenero, F.; Bonales, L.J.; Cobos, J.; Timón, V. Density Functional Theory Study of the Thermodynamic and Raman Vibrational Properties of $\gamma\text{-UO}_3$ Polymorph. *J. Phys. Chem. C* **2017**, *121*, 14507–14516. [[CrossRef](#)]
31. Colmenero, F.; Bonales, L.J.; Cobos, J.; Timón, V. Thermodynamic and mechanical properties of rutherfordine mineral based on density functional theory. *J. Phys. Chem. C* **2017**, *121*, 5994–6001. [[CrossRef](#)]
32. Colmenero, F.; Timón, V. Study of the structural, vibrational and thermodynamic properties of natroxalate mineral using density functional theory. *J. Solid State Chem.* **2018**, *263*, 131–140. [[CrossRef](#)]
33. Weck, P.F.; Gordon, M.E.; Greathouse, J.A.; Bryan, C.R.; Meserole, S.P.; Rodriguez, M.A.; Payne, M.C.; Kim, E. Infrared and Raman spectroscopy of $\alpha\text{-ZrW}_2\text{O}_8$: A comprehensive density functional perturbation theory and experimental study. *J. Raman. Spectrosc.* **2018**, *49*, 1373–1384. [[CrossRef](#)]
34. Malakkal, L.; Prasad, A.; Oladimeji, D.; Jossou, E.; Ranasinghe, J.; Szpunar, B.; Bichler, L.; Szpunar, J. Atomistic and experimental study on thermal conductivity of bulk and porous cerium dioxide. *Sci. Rep.* **2019**, *9*, 6326. [[CrossRef](#)]
35. Colmenero, F.; Plášil, J.; Sejkora, J. The crystal structures and mechanical properties of the uranyl carbonate minerals roubaultite, fontanite, sharpite, widenmannite, grimselite and cejkaite. *Inorg. Chem. Front.* **2020**, *7*, 4197–4221. [[CrossRef](#)]
36. Colmenero, F. Thermodynamic properties of the uranyl carbonate minerals roubaultite, fontanite, widenmannite, grimselite, cejkaite and bayleyite. *Inorg. Chem. Front.* **2020**, *7*, 4160–4179. [[CrossRef](#)]
37. Troullier, N.; Martins, J.L. Efficient Pseudopotentials for Plane-Wave Calculations. *Phys. Rev. B* **1991**, *43*, 1993–2006. [[CrossRef](#)]
38. Pfrommer, B.G.; Cote, M.; Louie, S.G.; Cohen, M.L. Relaxation of Crystals with the Quasi-Newton Method. *J. Comput. Phys.* **1997**, *131*, 233–240. [[CrossRef](#)]
39. Monkhorst, H.J.; Pack, J.D. Special Points for Brillouin-zone Integration. *Phys. Rev. B* **1976**, *13*, 5188–5192. [[CrossRef](#)]
40. Yu, R.; Zhu, J.; Ye, H.Q. Calculations of Single-Crystal Elastic Constants Made Simple. *Comput. Phys. Commun.* **2010**, *181*, 671–675. [[CrossRef](#)]
41. Colmenero, F.; Cobos, J.; Timón, V. Periodic DFT Study of the Structure, Raman Spectrum and Mechanical Properties of Schoepite Mineral. *Inorg. Chem.* **2018**, *57*, 4470–4481.
42. Colmenero, F.; Plášil, J.; Sejkora, J. The Layered Uranyl Silicate Mineral Uranophane- β : Crystal Structure, Mechanical Properties, Raman Spectrum and Comparison with the α -Polymorph. *Dalton Trans.* **2019**, *48*, 16722–16736. [[CrossRef](#)] [[PubMed](#)]
43. Grimme, S. Semiempirical GGA-type Density Functional Constructed with a Long-Range Dispersion Correction. *J. Comput. Chem.* **2006**, *27*, 1787–1799. [[CrossRef](#)] [[PubMed](#)]
44. Adamo, C.; Barone, V. Toward reliable density functional methods without adjustable parameters: The PBE0 model. *J. Chem. Phys.* **1999**, *110*, 6158–6170. [[CrossRef](#)]
45. Lee, C.; Yang, W.; Parr, R.G. Development of the Colle–Salvetti correlation-energy formula into a functional of the electron density. *Phys. Rev. B* **1988**, *37*, 785–789. [[CrossRef](#)]
46. Downs, R.T.; Bartelmehs, K.L.; Gibbs, G.V.; Boisen, M.B. Interactive Software for Calculating and Displaying X-Ray or Neutron Powder Diffractometer Patterns of Crystalline Materials. *Am. Mineral.* **1993**, *78*, 1104–1107.
47. Wang, Y.; Stucky, G.D.; Williams, J.M. Is squaric acid square? A Combined X-Ray and Neutron Diffraction Study of 3,4-Dihydroxycyclobut-3-ene-1,2-dione. *J. Chem. Soc. Perkin Trans.* **1974**, *2*, 35–38. [[CrossRef](#)]
48. Mouhat, F.; Coudert, F.X. Necessary and Sufficient Elastic Stability Conditions in Various Crystal Systems. *Phys. Rev. B* **2014**, *90*, 224104. [[CrossRef](#)]
49. Marmier, A.; Lethbridge, Z.A.D.; Walton, R.I.; Smith, C.W.; Parker, S.C.; Evans, K.E. EIAM: A Computer Program for the Analysis and Representation of Anisotropic Elastic Properties. *Comput. Phys. Commun.* **2010**, *181*, 2102–2115. [[CrossRef](#)]